



Article

Refractive Index Sensor Based on the Fano Resonance in Metal–Insulator–Metal Waveguides Coupled with a Whistle-Shaped Cavity

Bo Li ^{1,2}, Huarong Sun ², Huinan Zhang ², Yuetang Li ², Junbin Zang ², Xiyuan Cao ², Xupeng Zhu ³, Xiaolong Zhao ^{4,*} and Zhidong Zhang ^{2,*} 

¹ School of Software, North University of China, Taiyuan 030051, China

² Key Laboratory of Instrumentation Science & Dynamic Measurement of Ministry of Education, North University of China, Taiyuan 030051, China

³ School of Physical Science and Technology, Lingnan Normal University, Zhanjiang 524048, China

⁴ School of Electrical and Control Engineering, North University of China, Taiyuan 030051, China

* Correspondence: zhaoxiaolong@nuc.edu.cn (X.Z.); zdzhang@nuc.edu.cn (Z.Z.)

Abstract: A plasmonic refractive index sensor based on surface plasmon polaritons (SPPs) that consist of metal–insulator–metal (MIM) waveguides and a whistle-shaped cavity is proposed. The transmission properties were simulated numerically by using the finite element method. The Fano resonance phenomenon can be observed in their transmission spectra, which is due to the coupling of SPPs between the transmission along the clockwise and anticlockwise directions. The refractive index-sensing properties based on the Fano resonance were investigated by changing the refractive index of the insulator of the MIM waveguide. Modulation of the structural parameters on the Fano resonance and the optics transmission properties of the coupled structure of two MIM waveguides with a whistle-shaped cavity were designed and evaluated. The results of this study will help in the design of new photonic devices and micro-sensors with high sensitivity, and can serve as a guide for future application of this structure.

Keywords: plasmonic; refractive index sensor; finite element method; Fano resonance; metal–insulator–metal



Citation: Li, B.; Sun, H.; Zhang, H.; Li, Y.; Zang, J.; Cao, X.; Zhu, X.; Zhao, X.; Zhang, Z. Refractive Index Sensor Based on the Fano Resonance in Metal–Insulator–Metal Waveguides Coupled with a Whistle-Shaped Cavity. *Micromachines* **2022**, *13*, 1592. <https://doi.org/10.3390/mi13101592>

Academic Editors: Libo Gao and Zhuoqing Yang

Received: 2 September 2022

Accepted: 21 September 2022

Published: 25 September 2022

Publisher's Note: MDPI stays neutral with regard to jurisdictional claims in published maps and institutional affiliations.



Copyright: © 2022 by the authors. Licensee MDPI, Basel, Switzerland. This article is an open access article distributed under the terms and conditions of the Creative Commons Attribution (CC BY) license (<https://creativecommons.org/licenses/by/4.0/>).

1. Introduction

Surface plasmon polaritons (SPPs) have the capability of overcoming the diffraction limit due to their energy evanescently confining in the perpendicular direction of the metal–insulator interference [1–3]. SPPs have been widely used in surface-enhanced Raman scattering, imaging, solar cells, sensors, optical filters [4–10], and so on. Recently, another new type of surface plasmon, Tamm plasmon modes in the metal-PhC cavity, has shown excellent performance in gas sensors and refractive index sensors due to its sensitivity to the environment and strong localization [11–13]. For the application of manipulating SPPs in chip-scale integration, metal–insulator–metal (MIM) waveguides are an excellent subwavelength photonic device [14,15]. A plasmonic interferometric biosensor based on MIM waveguides for phase-sensitive biomolecular analysis has been proposed [16]. SPP photonic devices based on MIM waveguides have received increasing attention, such as all-optical switches, sensors, and slow light devices [17–19].

Recently, the Fano resonance phenomenon was observed in the MIM waveguide-coupled resonator system [20,21]. It was first discovered by Fano Ugo, and has an asymmetric line profile due to the interference between a narrow discrete resonance and a broad spectral line or continuum [22–24]. Fano resonance, as a weak coupling and interference phenomenon, has a unique line shape, which provides a promising pathway to achieve ultrahigh sensitivity sensors, lasing, all-optical switching, and nonlinear and slow

light [25–31]. Biosensors and chemical sensors based on Fano resonance have attracted much attention from researchers due to their extreme sensitivity to changes in structural parameters and the surrounding dielectrics [32,33]. These sensors exhibit good performance in terms of sensitivity and figure of merit (FOM) [34,35]. To achieve ultrahigh sensitivity, these structures and parameters need to be optimized. Therefore, the way in which to optimize the MIM waveguide-coupled resonator system to obtain a plasmonic coupled system with a Fano line shape is a key issue for designing high-sensitivity plasmonic sensors.

In this study, a whistle-shaped plasmonic structure composed of one whistle-shaped cavity and an MIM waveguide was designed to obtain high-sensitivity sensors based on Fano resonance. The transmission properties and magnetic field distributions of the whistle-shaped structures were simulated using the finite element method (FEM). The effects of the structural parameters of the whistle-shaped structure on the transmission spectrum were investigated. The refractive index sensitivity and the FOM of the whistle-shaped structure were explored. A derived plasmonic structure composed of a double whistle-shaped coupled structure was designed and evaluated. The sensitivity of the derived structure was examined.

2. Structure Model and Analytical Method

As shown in Figure 1a, the 2D schematic of the proposed plasmonic structure is composed of a whistle-shaped cavity and an MIM waveguide. The whistle-shaped cavity was composed of the input MIM waveguide on-interval and a ring cavity. As shown in Figure 1, the blue and white parts denote Ag (ϵ_m) and air (ϵ_s), respectively. The widths w of these MIM waveguides were fixed at 50 nm to support the only fundamental transverse magnetic (TM_0) in the MIM waveguides. The length of the output MIM waveguide is L , and the gap between the output MIM waveguide and the ring cavity is d_1 . The inner and outer radii of the ring cavity in the whistle-shaped structure are represented by r_1 and r_3 , and the center radius of the ring cavity is $r_2 = (r_1 + r_3)/2$. The red vertical dashed line passes through the center of the ring cavity and is defined as the reference line.

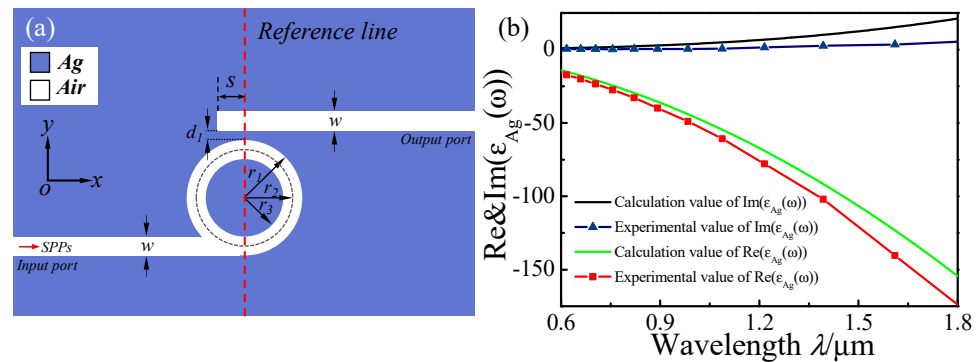


Figure 1. (a) Two-dimensional schematic for the MIM waveguides coupled with a whistle-shaped cavity. (b) The calculated and experimental values of the real and imaginary parts of the permittivity of silver.

The frequency-dependent complex relative permittivity $\epsilon(\omega)$ of silver is characterized by the modified Debye–Drude dispersion mode [36,37] as follows:

$$\epsilon(\omega) = \frac{\epsilon_\infty + (\epsilon_s - \epsilon_\infty)}{1 + i\omega\tau} + \frac{\sigma}{i\omega\epsilon_0} \quad (1)$$

where $\epsilon_\infty = 3.8344$ is the infinite frequency permittivity, $\epsilon_s = -9530.5$ represents the static permittivity, $\sigma = 1.1486 \times 10^7$ S/m is the conductivity, and $\tau = 7.35 \times 10^{-15}$ s is the relaxation time. Figure 1b shows the real part and the image part of the experiment value

and modified value using the Debye–Drude model for the silver relative permittivity. The theory mode is in good agreement with the experimental data.

The transmission properties of the single whistle-shaped structure and the double whistle-shaped coupled derived structure were investigated using FEM with perfectly matched layer-absorbing boundary conditions. The transmittance is defined as $T = |S_{21}|^2$, where S_{21} is the transmittance of the MIM waveguide [38].

For MIM waveguides, only the fundamental transverse magnetic (TM_0) mode can be supported, and its dispersion relation is expressed as [39]:

$$\tanh(\kappa w) = -2\kappa p \alpha / (\kappa^2 + p^2 \alpha^2) \quad (2)$$

where κ and w are the perpendicular core wave vector and the insulator width of the MIM waveguide, respectively. The symbols in Equation (1) are defined as $p = \epsilon_{in} / \epsilon_m$ and $\alpha = [k_0^2(\epsilon_{in} - \epsilon_m) + \kappa]^2$, where ϵ_{in} and ϵ_m are the dielectric constants of the insulator and the metal, respectively; $k_0 = 2\pi / \lambda_0$ is the free space wave vector; κ can be solved from Equation (1) using the iterative method. Thus, the effective index n_{eff} of the MIM waveguide can be defined as $n_{eff} = (\epsilon_m + (\kappa/k_0)^2)^{1/2}$. The wavelength of SPPs, λ_{spp} , can be expressed as $\lambda_{spp} = \lambda_0 / \text{Re}(n_{eff})$, where $\text{Re}(n_{eff})$ is the real part of n_{eff} .

3. Results and Discussions

Figure 2a shows the transmission spectrum of the whistle-shaped MIM waveguide system with $s = 30$ nm, $w = 50$ nm, $d = 10$ nm, and $r_2 = 145$ nm. As shown in Figure 2a, three asymmetrical profile peaks (0.645, 1.15, and 1.24 μm) can be observed in the transmission spectrum, which are regarded as the Fano resonance. The transmittance shows an unusual variation with the increase in wavelength from 1.15 to 1.24 μm ; in particular, a steep slope curve can be observed in the transmission spectrum at the range of 1.225–1.24 μm . The H_z field distributions at $\lambda = 0.645$, 1.15, 1.225, and 1.24 μm were simulated and are displayed in Figure 2b–e to understand the physical mechanism of the asymmetrical profile peaks of the proposed structure. Steady stand wave modes can be observed, and the black arrows represent the time-average power flow distributions in the H_z field distribution graphs. For $\lambda = 0.645$ μm , $\text{Re}(n_{eff}) = 1.4435$, and $\lambda_{spp} = 0.4468$ μm , so the number of wave nodes can be calculated by $2\pi r_2 / \lambda_{spp} = 2$. As shown in Figure 2b, two wave nodes were formed in the H_z field distribution, and the time-average power flow distributions show an anticlockwise mode in the ring cavity. Most of the SPPs' energy was limited in the whistle-shaped cavity, and part of the SPPs' energy was coupled into the output waveguide, so a peak was formed in the transmission spectrum, as shown in Figure 2a. For $\lambda = 1.24$ μm , the Fano resonance was caused by the interference between the anticlockwise mode and the clockwise mode. The H_z field distribution (Figure 2e) is similar to Figure 2d ($\lambda_2 = 1.225$ μm), but the SPPs' energy could be coupled into the output waveguide and a resonance peak is formed in the transmission spectrum for $\lambda_1 = 1.24$ μm . For $\lambda_2 = 1.225$ μm , the SPPs' energy was not coupled into the output waveguide. The time-average power flows show that an anticlockwise mode occurred. For $\lambda_3 = 1.15$ μm , the H_z field distribution was mainly distributed in the whistle-shaped cavity, and part of SPPs was coupled into the output waveguide. The time-average power flows show a clockwise mode. Thus, the Fano resonance was due to the coupling between the anticlockwise and clockwise modes. For $\lambda_4 = 0.645$ μm , the H_z field distribution reveals that a second-order vibration mode was formed in the whistle-shaped cavity, which was a new vibration mode. The time-average power flows show an anticlockwise mode.

The transmission spectra were simulated by replacing the air of the MIM waveguide system with different refractive index media ($n = 1, 1.33, 1.34$, and 1.35), which are shown in Figure 3a, to investigate the effect of refractive index n on the transmission properties of the whistle-shaped MIM waveguide system. As shown in Figure 3a, the Fano resonance peak red shifted with the increase in n , and another new resonance peak can be observed at the short wavelength range when n was larger than 1.33. The radius r_2 of the whistle-shaped cavity was fixed because the n_{eff} value in the MIM waveguide-coupled whistle-shaped

cavity decreased with the increase in n , and the number of modes increased. Therefore, a peak can be observed at the near short wave (0.60–0.7 μm) in the transmission spectra. We calculated the shift of the Fano resonance peaks (I and II) with the refractive index change. The sensitivity fitting curves of peaks I and II are shown in Figure 3b. The sensitivity of peak I is $S_1 = \delta\lambda/\delta n = 600 \text{ nm/RIU}$, and the sensitivity of peak II is $S_2 = \delta\lambda/\delta n = 1229 \text{ nm/RIU}$.

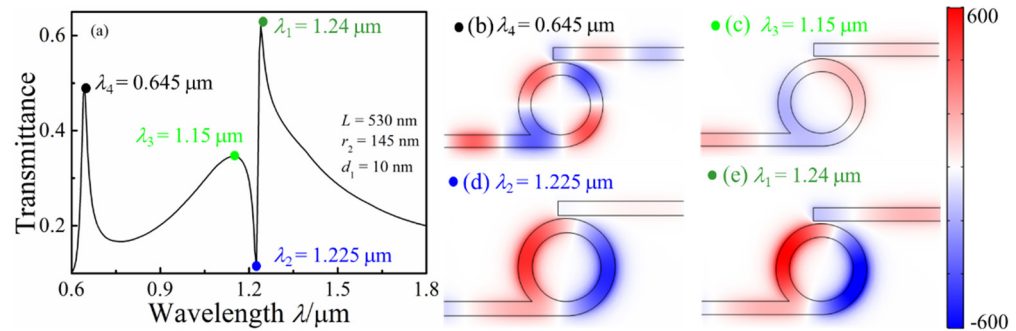


Figure 2. (a) Transmission spectra of the MIM waveguide-coupled whistle-shaped cavity; (b) contour profiles of the normalized H_z field distributions of the MIM waveguide whistle-shaped cavity: (b) $\lambda = 0.645 \text{ nm}$, (c) $\lambda = 1.15 \text{ nm}$, (d) $\lambda = 1.225 \text{ nm}$, and (e) $\lambda = 1.24 \text{ nm}$.

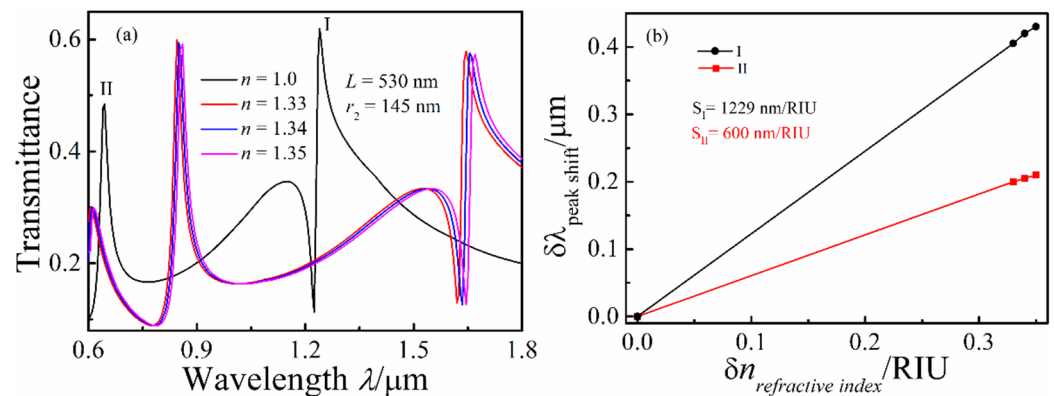


Figure 3. (a) Transmission spectra of the MIM waveguide-coupled whistle-shaped cavity with changing n ; (b) shift of the Fano resonance peak as a function of the refractive index change δn .

r_1 was varied from 130 to 170 nm at intervals of 10 nm with $n = 1$, $w = 50 \text{ nm}$, and $L = 530 \text{ nm}$ to study the effect of the different radii of the ring cavity on the Fano resonance of the MIM waveguide. With the increasing radius r_2 of the ring cavity, red shifts of the transmission spectrum and decreases in the transmittances of the Fano resonance peak can be observed in Figure 4a. Figure 4b shows the transmission spectrum with different coupled distances d between the top waveguide and the whistle-shaped ring cavity, and the other parameters were fixed as $n = 1$, $r_1 = 150 \text{ nm}$, $r_3 = 100 \text{ nm}$, and $d_1 = 10 \text{ nm}$. From the transmission spectrum, the Fano resonance peak appears to be blue-shifted, but this was actually caused by the Fano resonance peak widening as d_1 increased, and the transmittances decreased with the increase in d_1 . In contrast, the Fano resonance valley hardly shifted with as d_1 increased, which was dependent on the length of the whistle-shaped ring cavity.

In this section, we investigate the derivative structure, MIM waveguide-coupled whistle-shaped cavity, and the proposed structure, as shown in Figure 5a. Figure 5b shows the transmission spectrum of the proposed MIM waveguide-coupled double whistle-shaped cavity, and the structural parameters were fixed at $n = 1$, $R_2 = r_2 = 125 \text{ nm}$, and $d_2 = 10 \text{ nm}$. Although the transmission spectrum is similar to the MIM waveguide-coupled single-whisper cavity, another new peak emerged in the transmission spectrum. FR_2 was unremarkable and FR_1 and FR_2 were extremely close when $R_2 = r_2$. The H_z field distri-

butions at $\lambda_1 = 1.09$ nm, $\lambda_2 = 1.06$ nm, $\lambda_3 = 1.05$ nm, $\lambda_4 = 1.045$ nm, and $\lambda_5 = 0.995$ nm are displayed in Figure 5c. For $\lambda_1 = 1.09$ nm, the phase of the H_z field distribution in the bottom and top whistle-shaped cavities was opposite, and the output waveguide was located at the position of the strong negative time-averaged power flow, so the SPPs' energy could be passed from the output waveguide. For $\lambda_2 = 1.06$ nm, the H_z field distribution in the bottom and top whistle-shaped cavities was symmetric on the vertical axis. The output waveguide was located at the position joint between the positive and negative time-averaged power flows, so few SPPs' energy could be passed. For $\lambda_3 = 1.05$ nm, the strong H_z field distribution concentrated in the bottom whistle-shaped cavity, and few SPPs' energy were coupled into the top whistle-shaped cavity. The output waveguide was located in the abdominal of the negative time-averaged power flow, so the SPPs' energy could be passed to the output waveguide. For $\lambda_4 = 1.045$ nm, the H_z field distribution in the bottom and top whistle-shaped cavities was located on the horizontal axis. For $\lambda_5 = 0.995$ nm, the strong H_z field was mainly distributed in the bottom whistle-shaped cavity, and few SPPs' energy were coupled into the top whistle-shaped cavity.

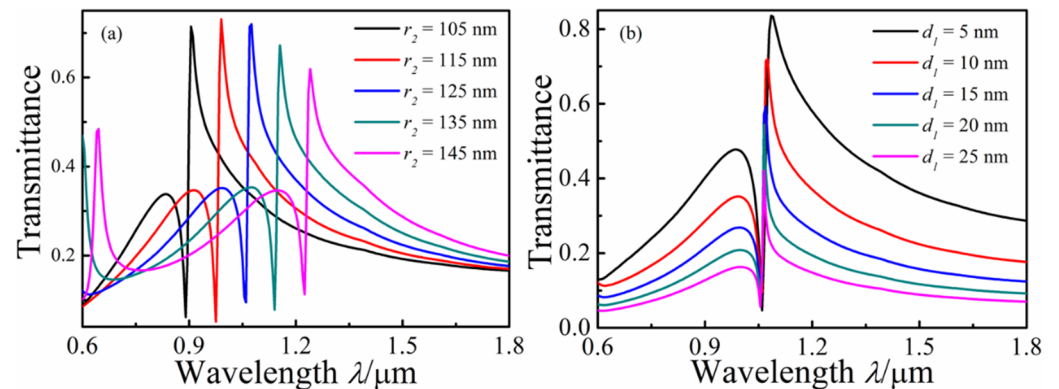


Figure 4. Transmission spectra of the MIM waveguide-coupled whistle-shaped cavity: (a) With changing r_2 ; (b) with changing d_1 .

The value of R_2 changed and was varied from 130 to 170 nm at intervals of 10 nm, with $r_1 = 150$ nm and $d_2 = 10$ nm, to further investigate the effect of the top whisper cavity on the Fano resonance. A remarkable double Fano resonance was found in the transmission spectra, as shown in Figure 6a. With the increase in R_2 , an obvious red shift can be observed in the transmission spectra. The locations of the FR_2 peak's red shift with the increase in R_2 and the transmittance of FR_2 first showed decreases and then increases. When $R_2 = r_2$, the transmittance was minimal, and with an increasing R_2 , new FR_3 peaks can be observed in the transmission spectra for $R_2 = 135$ nm. From Figure 6b, FR_1 seems to be blue-shifted, but this was actually due to a decrease in the peak width of FR_1 with the increase in the distance (d_2) between the ring cavity from 5 to 25 nm when the values of R_2 and r_2 were fixed as 125 nm. The transmittance of FR_2 decreased, but FR_2 experienced no shift with as d_2 increased. When $d_2 = 25$ nm, the peak of FR_2 disappeared in the transmission spectra. With an increasing d_2 , FR_3 was blue-shifted and the transmittance decreased. Figure 6c shows the transmittance spectrum when changing its refractive index n ($n = 1, 1.33, 1.34$, and 1.35) of the proposed double whisper cavities, and the other parameters were fixed as $d_2 = 10$ nm, $r_2 = 125$ nm, and $R_2 = 115$ nm. The Fano resonance exhibited a red shift with the increase in the refractive index n , and the sensitivities of $1.057 \mu\text{m}/\text{RIU}$ and $0.969 \mu\text{m}/\text{RIU}$ were obtained at $\lambda_1(FR_1)$ and $\lambda_2(FR_2)$.

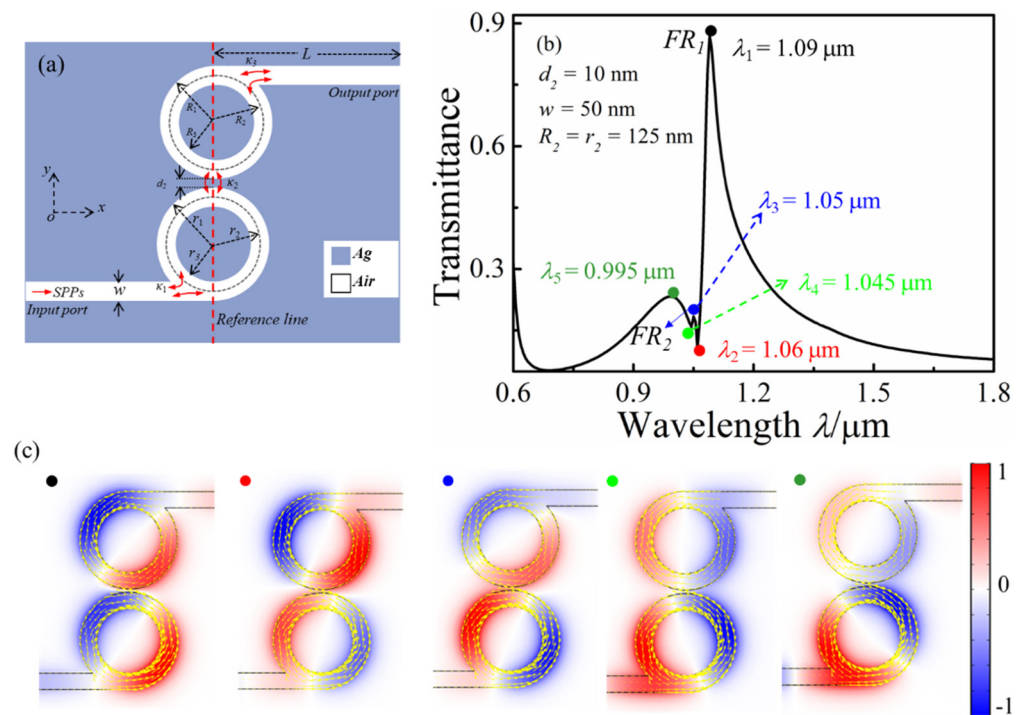


Figure 5. (a) Schematic of the MIM waveguide-coupled double whisper cavities; (b) transmission spectrum of the double whisper cavity structure; (c) H_z field distribution at different resonance wavelengths.

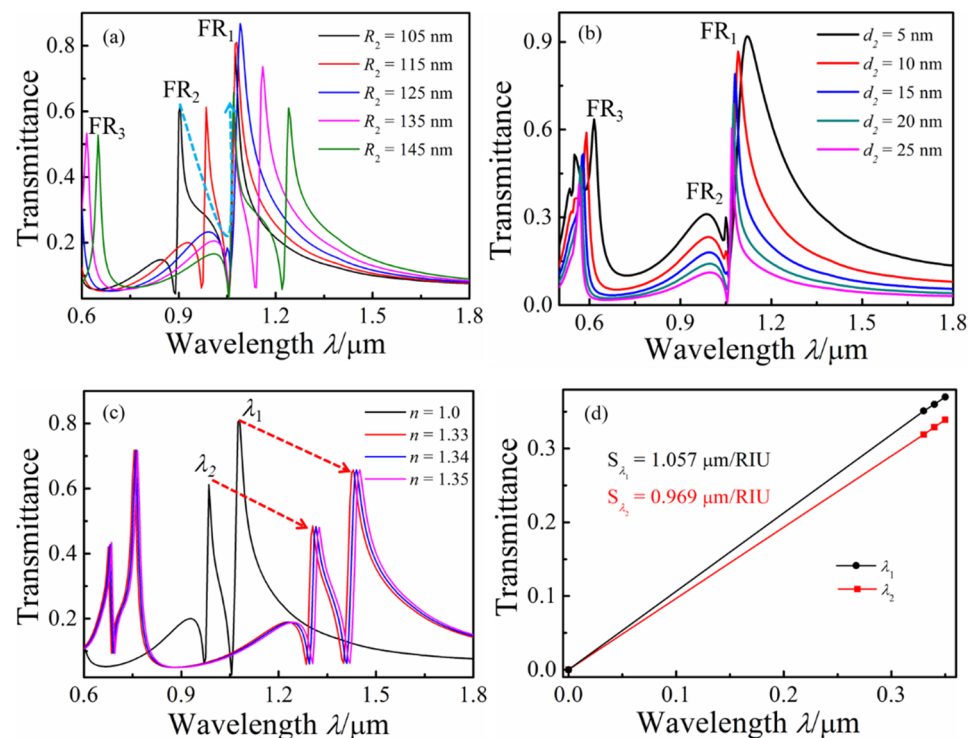


Figure 6. Transmission spectra of the different structural parameters at the MIM waveguide-coupled double whistle-shaped cavities: (a) R_2 changing; (b) d_2 changing; (c) n changing; (d) sensitivity.

4. Conclusions

In this work, a plasmonic refractive index sensor based on Fano resonance was proposed. The transmission properties were simulated numerically using FEM. Fano resonance was realized in the MIM waveguide-coupled whistle-shaped cavity. This phenomenon is

due to the coupling of SPPs in the whistle-shaped cavity between the transmission along the clockwise and anticlockwise directions. Refractive index-sensing based on the Fano resonance was investigated by changing the refractive index of the insulator of the MIM waveguide. The results showed that a maximum sensitivity of 1229 RIU/nm was obtained. Compared to the single MIM waveguide-coupled whistle-shaped cavity, the double MIM with whistle-shaped cavity structure exhibited multi-Fano resonance. The refractive index sensor's sensitivity was smaller than that of the single MIM waveguide-coupled whistle-shaped cavity. The results of this study will help in the design of new photonic devices and microsensors with high sensitivity.

Author Contributions: Conceptualization, Z.Z. and B.L.; methodology, X.Z. (Xiaolong Zhao); software, H.S.; validation, Y.L. investigation, J.Z.; data curation, B.L. and H.Z.; writing—original draft preparation, B.L. and H.S.; writing—review and editing, Z.Z., X.Z. (Xupeng Zhu) and X.C. All authors have read and agreed to the published version of the manuscript.

Funding: This work was funded by the Key Research and Development Program of Shanxi Province (No. 202102030201008), the National Natural Science Foundation of China (No. 12004150), the Fundamental Research Program of Shanxi Province (No. 201901D111148), and the Scientific and Technological Innovation Programs of Higher Education Institutions in Shanxi (No. 2020L0275).

Data Availability Statement: The data presented in this study are available upon request from the corresponding author. The data are not publicly available due to being supplied by Key Laboratory of Instrumentation Science & Dynamic Measurement (North University of China), Ministry of Education, and so cannot be made freely available.

Conflicts of Interest: The authors declare no conflict of interest.

References

1. Barnes, W.L.; Dereux, A.; Ebbesen, T.W. Surface plasmon subwavelength optics. *Nature* **2003**, *424*, 824–830. [[CrossRef](#)] [[PubMed](#)]
2. Ozbay, E. Plasmonics: Merging Photonics and Electronics at Nanoscale Dimensions. *Science* **2006**, *311*, 189–193. [[CrossRef](#)] [[PubMed](#)]
3. Fang, Y.; Sun, M. Nanoplasmonic waveguides: Towards applications in integrated nanophotonic circuits. *Light-Sci. Appl.* **2015**, *4*, e294. [[CrossRef](#)]
4. Chen, J.; Sun, C.; Rong, K.; Li, H.; Gong, Q. Polarization-free directional coupling of surface plasmon polaritons. *Light-Sci. Appl.* **2015**, *9*, 419–426. [[CrossRef](#)]
5. Zhang, X.; Liu, Z. Superlenses to overcome the diffraction limit. *Nat. Mater.* **2008**, *7*, 435–441. [[CrossRef](#)] [[PubMed](#)]
6. Green, M.A.; Pillai, S. Harnessing plasmonics for solar cells. *Nat. Photonics* **2012**, *6*, 130–132. [[CrossRef](#)]
7. Zhou, F.; Qin, F.; Yi, Z.; Yao, W.T.; Liu, Z.; Wu, X.; Wu, P. Ultra-wideband and wide-angle perfect solar energy absorber based on Ti nanorings surface plasmon resonance. *Phys. Chem. Chem. Phys.* **2021**, *23*, 17041–17048. [[CrossRef](#)]
8. Zhao, F.; Lin, J.; Lei, Z.; Yi, Z.; Qin, F.; Zhang, J.; Liu, L.; Wu, X.; Yang, W.; Wu, P. Realization of 18.97% theoretical efficiency of 0.9 μm Thick c-Si/ZnO Heterojunction Ultrathin-film Solar Cells via Surface Plasmon Resonance Enhancement. *Phys. Chem. Chem. Phys.* **2022**, *24*, 4871–4880. [[CrossRef](#)]
9. Joo, Y.H.; Song, S.H.; Magnusson, R. Demonstration of long-range surface plasmon-polariton waveguide sensors with asymmetric double-electrode structures. *Appl. Phys. Lett.* **2010**, *97*, 201105. [[CrossRef](#)]
10. Zhao, L.; Zhang, X.; Wang, J.; Yu, W.H.; Li, J.D.; Su, H.; Shen, X.P. A Novel Broadband Band-pass Filter Based on Spoof Surface Plasmon Polaritons. *Sci. Rep.* **2016**, *6*, 36069. [[CrossRef](#)]
11. Zaky, Z.A.; Singh, M.R.; Aly, A.H. Tamm resonance excited by different metals/graphene. *Photonic. Nanostruct.* **2022**, *49*, 100995. [[CrossRef](#)]
12. Zaky, Z.A.; Singh, M.R.; Aly, A.H. Tamm Plasmon Polariton as Refractive Index Sensor Excited by Gyroid Metals/Porous Ta₂O₅ Photonic Crystal. *Plasmonics* **2022**, *17*, 681–691. [[CrossRef](#)]
13. Li, L.; Hao, H.Y. Evolution of high-order Tamm plasmon modes with a metal-PhC cavity. *Sci. Rep.* **2022**, *12*, 14921. [[CrossRef](#)] [[PubMed](#)]
14. Han, Z. Ultracompact plasmonic racetrack resonators in metal-insulator-metal waveguides. *Photonic. Nanostruct.* **2010**, *8*, 172–176. [[CrossRef](#)]
15. Makarenko, K.S.; Hoang, T.X.; Duffin, T.J.; Radulescu, A.; Kalathingal, V.; Lezec, H.J.; Chu, H.S.; Nijhuis, C.A. Efficient Surface Plasmon Polariton Excitation and Control over Outcoupling Mechanisms in Metal-Insulator-Metal Tunneling Junctions. *Adv. Sci.* **2020**, *7*, 1900291. [[CrossRef](#)]
16. Kozma, P.; Kehl, F.; Ehrentreich-Forster, E.; Stamm, C.; Bier, F.F. Integrated planar optical waveguide interferometer biosensors: A comparative review. *Biosens. Bioelectron.* **2014**, *58*, 287–307. [[CrossRef](#)]

17. Tian, M.; Lu, P.; Chen, L.; Liu, D.M.; Lv, C. All-optical switching in MIM waveguide resonator with an outer portion smooth bend structure containing nonlinear optical materials. *Opt. Commun.* **2012**, *285*, 4562–4566. [[CrossRef](#)]
18. Pang, S.F.; Huo, Y.P.; Xie, Y.; Hao, L.M. Fano resonance in MIM waveguide structure with oblique rectangular cavity and its application in sensor. *Opt. Commun.* **2016**, *381*, 409–413. [[CrossRef](#)]
19. Wang, G.X.; Lu, H.; Liu, X.M. Dispersionless slow light in MIM waveguide based on a plasmonic analogue of electromagnetically induced transparency. *Opt Express* **2012**, *20*, 20902–20907. [[CrossRef](#)]
20. Wen, K.H.; Hu, Y.H.; Chen, L.; Zhou, J.Y.; He, M.; Lei, L.; Meng, Z.M.; Wu, Y.J.; Li, J.F. Fano Resonance Based on End-Coupled Cascaded-Ring MIM Waveguides Structure. *Plasmonics* **2017**, *12*, 1875–1880. [[CrossRef](#)]
21. Yun, B.F.; Zhang, R.H.; Hu, G.H.; Cui, Y.P. Ultra Sharp Fano Resonances Induced by Coupling between Plasmonic Stub and Circular Cavity Resonators. *Plasmonics* **2016**, *11*, 1157–1162.
22. Fano, U. Effects of configuration interaction on intensities and phase shifts. *Phys. Rev.* **1961**, *124*, 1866–1878. [[CrossRef](#)]
23. Khanikaev, A.B.; Wu, C.H.; Shvets, G. Fano-resonant metamaterials and their applications. *Nanophotonics* **2013**, *2*, 247–264. [[CrossRef](#)]
24. Limonov, M.F.; Rybin, M.V.; Poddubny, A.N.; Kivshar, Y.S. Fano resonances in photonics. *Nat. Photonics* **2017**, *11*, 543–554. [[CrossRef](#)]
25. Stern, L.; Grajower, M.; Levy, U. Fano resonances and all-optical switching in a resonantly coupled plasmonic–atomic system. *Nat. Commun.* **2014**, *5*, 4865. [[CrossRef](#)]
26. Deng, Z.L.; Dong, J.W. Lasing in plasmon-induced transparency nanocavity. *Opt. Express* **2013**, *21*, 20291–20302. [[CrossRef](#)]
27. Wu, C.H.; Khanikaev, A.B.; Adato, R.; Arju, N.; Yanik, A.A.; Altug, H.; Shvets, G. Fano-resonant asymmetric metamaterials for ultrasensitive spectroscopy and identification of molecular monolayers. *Nat. Mater.* **2012**, *11*, 69–75. [[CrossRef](#)]
28. Wu, C.H.; Khanikaev, A.B.; Shvets, G. Broadband Slow Light Metamaterial Based on a Double-Continuum Fano Resonance. *Phys. Rev. Lett.* **2011**, *106*, 107403. [[CrossRef](#)]
29. Zhang, F.; Hu, X.Y.; Zhu, Y.; Yang, H.; Gong, Q.H. Ultralow-power all-optical tunable dual Fano resonances in nonlinear metamaterials. *Appl. Phys. Lett.* **2013**, *103*, 191116. [[CrossRef](#)]
30. Deng, Y.; Cao, G.T.; Yang, H. Tunable Fano resonance and high-sensitivity sensor with high figure of merit in plasmonic coupled cavities. *Photonic. Nanostruct.* **2018**, *28*, 45–51. [[CrossRef](#)]
31. Zhang, Y.J.; Kuang, Y.Q.; Zhang, Z.D.; Tang, Y.; Han, J.Q.; Wang, R.B.; Cui, J.G.; Hou, Y.L.; Liu, W.Y. High-sensitivity refractive index sensors based on Fano resonance in the plasmonic system of splitting ring cavity-coupled MIM waveguide with tooth cavity. *App. Phys. A* **2019**, *125*, 13. [[CrossRef](#)]
32. Lotfiani, A.; Mohseni, S.M.; Ghanaatshoar, M. High-sensitive optoelectronic SPR biosensor based on Fano resonance in the integrated MIM junction and optical layers. *Opt. Commun.* **2020**, *477*, 126323. [[CrossRef](#)]
33. Deng, Y.; Cao, G.T.; Yang, H.; Li, G.H.; Chen, X.S.; Lu, W. Tunable and high-sensitivity sensing based on Fano resonance with coupled plasmonic cavities. *Sci. Rep.* **2017**, *7*, 10639. [[CrossRef](#)] [[PubMed](#)]
34. Lan, G.Q.; Liu, S.G.; Ma, Y.; Zhang, X.R.; Wang, Y.X.; Song, Y.L. Sensitivity and figure-of-merit enhancements of liquid-prism SPR sensor in the angular interrogation. *Opt. Commun.* **2015**, *352*, 49–54. [[CrossRef](#)]
35. Chen, H.; Chen, Z.; Yang, H.; Wen, L.; Yi, Z.; Zhou, Z.; Dai, B.; Zhang, J.; Wu, X.; Wu, P. Multi-mode surface plasmon resonance absorber based on dart-type single-layer graphene. *RSC Adv.* **2022**, *12*, 7821–7829. [[CrossRef](#)] [[PubMed](#)]
36. Zayats, A.V.; Smolyaninov, I.I.; Maradudin, A.A. Nano-optics of surface plasmon polaritons. *Phys. Rep.* **2005**, *408*, 131–314. [[CrossRef](#)]
37. Gai, H.; Wang, J.; Tian, Q. Modified Debye model parameters of metals applicable for broadband calculations. *Appl. Opt.* **2007**, *46*, 2229–2233. [[CrossRef](#)]
38. Zhang, Z.D.; Luo, L.; Xue, C.Y.; Zhang, W.D.; Yan, S.B. Fano Resonance Based on Metal-Insulator-Metal Waveguide-Coupled Double Rectangular Cavities for Plasmonic Nanosensors. *Sensors* **2016**, *16*, 642. [[CrossRef](#)]
39. Zhang, Z.Y.; Wang, J.D.; Zhao, Y.A.; Lu, D.; Xiong, Z.H. Numerical investigation of a branch-shaped filter based on metal-insulator-metal waveguide. *Plasmonics* **2011**, *6*, 773. [[CrossRef](#)]